Combining single-molecule super-resolved localization microscopy with fluorescence polarization imaging to study cellular processes

Jack W Shepherd[1,2,3], Alex L Payne-Dwyer[1,2,3], and Mark C Leake[1,2]*

[1]Department of Physics, University of York, York, YO10 5DD

[2]Department of Biology, University of York, York, YO10 5DD

[3]These authors contributed equally

*To whom correspondence should be addressed. E-mail mark.leake@york.ac.uk

Abstract

Super-resolution microscopy has enabled valuable insights into the subcellular, mechanistic details of many different biological processes across a wide range of cell types. Fluorescence polarization spectroscopy tools have also enabled important insights into cellular processes through identifying orientational changes of biological molecules typically at an ensemble level. Here, we combine these two biophysical methodologies in a single home-made instrument to enable the simultaneous detection of orthogonal fluorescence polarization signals from single fluorescent protein molecules used as common reporters on the localization on biomolecules in cellular processes, whose spatial location can be pinpointed to a super-resolved precision better than the diffraction-limited optical resolution. In this small innovation we have adapted a millisecond timescale "Slimfield" microscope used for single-molecule detection to enable spitting of the fluorescence polarization emissions into two separate imaging channels for *s*- and *p*- polarization signals that are imaged onto separate halves of the same high sensitivity back-illuminated CMOS camera detector. We applied this fluorescence polarization super-resolved imaging modality to a range of test fluorescent samples relevant to the study of biological processes, including purified monomeric green fluorescent protein (mGFP). Our findings are largely qualitative but demonstrate promise in showing how fluorescence polarization and Slimfield-mediated super-resolved localization microscopy can be combined on the same sample to enable new biological insights.

Introduction

Understanding the 'physics of life' at the molecular level [1] has undergone a revolution since the development and refinement of fluorescence microscopy [2] and is now routinely used at millisecond timescales to understand the spatial organization within living cells as well as the dynamical properties of constituent biomolecules [3]. In particular, the mobility – both translational and rotational - of these biomolecules gives information on their local cellular environment and their functional interactions, i.e. *which* molecules interact with other molecules inside cells, *where* they interact in the context of their subcellular location, and *when* they interact in the context of past and future biological events. While translational diffusion coefficients [4] or molecular dynamics simulations [5] can be used to estimate rotational properties of biomolecules, intracellular environments are crowded, with values of ~20% (w/v) protein content or more being typical [6], and present complex diffusive landscapes in which states of rotational and translational mobility are not necessarily indicative of one another [7]. More accurate experimental measurements of rotational

states are desirable, especially if coupled with the simultaneous ability to resolve spatially where in a living cell these rotating biological molecules are.

Fluorescent 'reporter' probes, i.e. fluorescent tags that report on the location of specific biological molecules, remain a powerful and selective tool in this regard. As the excited molecule collapses to its ground state and radiates, the emitted photon's electric field aligns with the transition electric dipole moment of the emitting fluorophore [8], leading to a well-defined linear polarization. With dedicated optical components in a microscope setup one may decompose the emission of individual fluorophores into orthogonal components, and measurement of their relative intensities confers information on the fluorophore's azimuthal angle about the optical axis of the instrument.

In the cell cytoplasm and other biologically relevant systems with relatively low orientation constraints, molecular rotation typically occurs on a nanosecond timescale, meaning that measurement of rotationally-coupled properties requires specialized photon counting hardware with extremely high temporal resolution [9]. This temporal accuracy however typically comes at the cost of poor spatial resolution, with nanosecond scale experiments usually performed at an ensemble detection scale equivalent to several thousands of molecules [10]. Where available, simultaneous high spatial and temporal resolutions enable detailed measurements of dynamical processes, such as in studies of conformational actuations of molecular motors [11] or lipid membrane components [12], though this is typically limited by a small imaging volume that precludes reconstructing an image of a biological cell on a relevant timescale. On the other hand, imaging diffusing molecules on millisecond timescales - at the sensitivity or readout limits of current fluorescence microscope cameras [13], [14] for fully sampled multi-micron fields of view - allows the molecule of interest to tumble hundreds or thousands of times during a single frame acquisition, effectively scrambling the polarization signal [15]. For strongly interacting molecules, such as those attached to a surface [8] or bound to other biomolecules [16], the rotational diffusion time increases and the range of accessible rotational states is greatly diminished so that the polarization signal is more easily detected. Similarly, molecules with a higher directional structural stability such as DNA intercalating dyes [17], [18], fibers [19] , or membrane proteins [20] show a strong polarization signal if care is taken not to depolarize the emitted light.

This effect can be harnessed widely on an ensemble scale in fluorescence anisotropy assays, commonly used for drug discovery [21] and studies of enzymatic binding [22] and nucleic acid conformations [23]. While anisotropy assays can be refined to a dilute single-molecule level *in vitro* [9] or to high sensitivity using strategies such as modulated input polarization [24], the fact remains that without detection of single molecular complexes in individual living cells, this approach can neither describe heterogeneous phenotypes across living populations, nor disentangle the dynamic microenvironments within each cell. However, polarization-sensitive imaging of individual live cells [25], [26] can be combined with single-molecule techniques [27], [28] which directly admit this level of discrimination, as previously used to remove bias from super-resolution reconstructions [29], [30]. These combined super-resolution techniques have been used to study dynamic events in macromolecule assembly with full molecular orientation reporting at a timescale of 100 ms [28], [31]–[33], although the requirement for total internal reflection renders this primarily suitable for surface-based imaging. Sophisticated theoretical treatments also exist for the unequivocal detection of molecular orientation in images [34], [35], though most require defocus or other image aberrations that are not ideal or intuitive for live imaging.

In our present work, we report a method to combine super-resolvable Slimfield microscopy [36] with polarization microscopy, in which demonstrate as proof-of-concept that we easily image single fluorophores with subpixel resolution at rapid exposure times of 40 ms, splitting the linear *s* and *p*

polarization components and imaging them simultaneously. The use of Slimfield microscopy means we are not limited to surface imaging and can therefore image biological structures *inside* cells when appropriate. The image stacks are analyzed with our in-house MATLAB software package called ADEMSCode [37] which identifies the super-resolved positions of the fluorophores, nominally to a spatial lateral precision of ~40 nm [38]. With post-processing software written in Python, we spatially register the two channels, and find the total intensity for each spot in both polarization channels, converting this into a polarization value, on a fluorescent molecule-by-molecule basis.

We demonstrate that under circularly polarized excitation, monomeric GFP (mGFP) either immobilized to a glass coverslip surface or diffusing freely in solution recovers the expected qualitative form of the polarization distribution.

Methods

Slimfield Microscopy

Slimfield microscopy was performed on a bespoke epifluorescence microscope described previously adapted for single-molecule detection with millisecond timescale sampling [39] . The excitation source was a continuous wave laser at 488 nm (Coherent Obis XS) with intrinsic vertical polarization. The settings were as follows for all experiments: source power 20 mW equivalent to approximately 8 kW/cm^2 at the sample after beam expansion and de-expansion (see Figure 1); exposure time per frame of 40 ms (i.e. framerate of 25 Hz). For experiments requiring circularly polarized excitation, a λ/4 waveplate (Thorlabs part AQWP05M-600) was placed in the laser delivery path prior to the microscope entrance pupil. The correct circularization was ensured by rotating the λ/4 waveplate to equalize the power transmitted through a linear polarizer in the sample plane, independently of the linear polarizer's direction. For experiments using linearly polarized excitation, this λ/4 waveplate was removed and replaced with a λ/2 wave plate (Thorlabs part AHWP05M-600) rotated by either 0° for vertical polarization or 45° for horizontal polarization at sample.

Polarization split detection

The polarization splitter module centred on a ratio polarizing beam splitter cube (Thorlabs PBS251), into whose downstream paths linear polarizing filters (Thorlabs LPVISA100) were placed to clean up traces of non-polarized light. All optical components were fixed to a magnetically mounted breadboard to allow the exchange of this module for the colour channel splitter usually in place. A schematic diagram of the polarization splitter can be seen in Figure 1.

GFP in vitro sample preparation

Monomeric green fluorescent protein (normal enhanced GFP but with the addition of an A206K point mutation to inhibit dimerization) was purified from competent *E. coli* as described previously [38]. Samples were prepared inside 'tunnel' slides with standard microscope slides, plasma cleaned #1.5 coverslips and double-sided sticky tape as described previously [40], [41]. Initially, the tunnel was washed with 100 µL of phosphate buffer saline (PBS, Sigma Aldrich), and then 10 µL of 10 µg/mL anti-GFP (RPCA-GFP, EnCor Biotechnology Inc.) was flowed in and incubated for 5 min. The antibodies form a sparse carpet on the plasma-cleaned coverslip surface for mGFP to bind to. Excess anti-GFP remining in solution was then washed out with 100 µL PBS, and the slide was then

incubated with 10 µL 1 mg/mL bovine serum albumin (BSA) (05479, Sigma-Aldrich) for 5 min to passivate the surface against non-specific binding of mGFP; weakly bound, transiently diffusing mGFP molecules could be a source of error in the analysis which presupposes either truly immobile or freely-diffusing fluorophores. After a further 100 µL PBS wash, 10 µL 50 ng/mL (2 nM) purified mGFP in PBS was flowed in and incubated for 5 min, to bind to the surface immobilized anti-GFP. A final 100 µL PBS wash was performed, the slide sealed with clear topcoat nail polish (Rimmel London) and imaged immediately. For mGFP in solution, the same procedure was used with the omission of the anti-GFP incubation step, and the final incubation/wash steps, and focusing a few microns into solution as opposed to on the coverslip surface itself as for surface immobilized mGFP. In this case, the BSA incubation passivates the entire surface and the mGFP therefore remain in solution for imaging of their diffusive behaviour. All incubations were performed with the slide inverted in a humidity chamber at ambient room temperature. A schematic diagram of the immobilized mGFP assay is shown in Figure 2.

Choice of polarization metric

The fluorescence polarization metric, ρ, is relatively intuitive and is well-defined within the range (-1,+1) for single detected fluorescent foci (the diffraction-limited point spread function in the microscope's focal plane).

$$\rho_V = \frac{I_{VS} - I_{VP}}{I_{VS} + I_{VP}}$$

$$\rho_H = \frac{I_{HS} - I_{HP}}{I_{HS} + I_{HP}}$$

$$\rho_C = \frac{I_{CS} - I_{CP}}{I_{CS} + I_{CP}} \approx \frac{\rho_V + \rho_H}{2}$$

Both the method presented here and standard anisotropy assays aim to measure the same fundamental property of fluorescence polarization, and so share the assumption that fluorophores are dipolar and act independently. However, there are non-trivial differences, including their assumptions about the number of emitters per measurement, or equivalently the stoichiometry S of a detected spot. Most of these assays describe ensemble measurements (S >> 1) of anisotropy, $r = 2\rho_V/(3 - \rho_V)$, with perpendicular axes of excitation and detection. Under Slimfield microscopy, the single- or few-emitter limit is important - within which the relevance of the anisotropy metric is unclear - and the optical axes of excitation and detection are colinear. With care, one may assess the theory used for routine assays, assuming the collective behavior of randomly oriented ensembles, to interpret the Slimfield polarization results. For example, the Perrin equation describes how under linear polarized excitation, the photoselected polarization signal decreases according to the rotation timescale τ_R, which is the property of interest in our experiments. It reads as:

$$\left(\frac{1}{\langle \rho_L \rangle} - C\right) = \left(\frac{1}{\rho_L'} - C\right)\left(1 + \frac{\tau_F}{\tau_R}\right)$$

where τ_F is the fluorescent lifetime and C = 1/3 in the ensemble limit (S >> 1) and the subscript L can refer to either V or H. The *fundamental polarization, ρ'*, describes the theoretical, integrated

response of many randomly oriented emitters of in the *absence* of rotational depolarization. The concept can be extended to single or few emitters, for which the expectation in general depends on the stoichiometry *S,* i.e. the number of independent emitters per focus. Under excitation that is parallel to one of the detection channels, the photoselection effect favors that channel and the expectations become $\rho'_V = (1 - 1/\sqrt{S})/2$ and $\rho'_H = -(1 - 1/\sqrt{S})/2$ respectively [42].

Under circularly polarized or unpolarized excitation, the situation appears rather different. The photoselection effect is equalized over both axes of the detector and the resulting expectation is unbiased, $\rho'_C = (\rho'_V + \rho'_H)/2 = 0$. However, the rotational decay of each measured non-zero polarization is inherently the same. Since anisotropy *r*, and not polarization *ρ*, is additive in the ensemble limit [21] , the apparent rotational timescale is related to the average of $(1+ \tau_F/\tau_R)^{-1}$ over the measurement time τ, which in this case is the camera exposure time of 40 ms.

As such, the polarization signal from an individual fluorescent focus provides a measure of the *fastest* rotational timescale of the emitters at that location. In the context of our experiment therefore, a focus with non-zero polarization signal indicates a set of molecules, within a super-resolvable localization, that are persistently constrained in their rotational dynamics over the full duration of the exposure.

In all cases, the measured polarization signal from our microscope instrumentation if applied to cell samples is also attenuated due to several depolarization factors. With colinear detection from a monolayer of cells, the contribution due to scattering is minimal. The largest contribution is expected to be the high numerical aperture (NA) of the objective, which distorts how polarization components in the sample plane couple to those in the excitation and detection paths. We note that in Slimfield, the excitation beam strongly underfills the back focal plane of the objective lens to emerge collimated, and therefore the incident laser itself will not be prone to depolarization from the lens' numerical aperture. However, the theoretical effect on depolarization of the fluorescence emission [43] reveals a similar form to the Perrin equation above:

$$\left(\frac{1}{\rho} - 1\right) = \left(\frac{1}{\rho_0} - 1\right)\left(\frac{2}{1 + \sin(2\psi)/2\psi}\right)$$

where ρ_0 is the underlying polarization in the limit NA = 0 and $\psi = \sin^{-1}(\mathrm{NA}/n)$ is the half angle of the detection, with *n* the refractive index of the objective's coupling medium. The effect is such that extreme polarizations remain accurate, but smaller polarization signals are suppressed by up to 40% at our NA=1.49.

A locally-variable contribution to depolarization is homo-FRET [44] , in which photoselected emitters transfer their energy to another nearby emitter, whose alignment has a weaker correlation with the absorbed photon. The net effect is to depolarize the emission at that particular location. As such, homo-FRET itself has been identified as a potential signature of protein aggregation, but it only occurs when the chromophores approach within a few nanometers, so the corresponding depolarization is a weak effect for relatively large fluorescent proteins.

For the work presented here, the above effects limit the ability to infer a quantitative molecular orientation, which would require a high degree of confidence in the corrections for depolarization. Instead, we look at population-scale measurements by summing the responses of individual fluorescent foci, themselves not inherently of single fluorophores if applied to live cell samples, to allow a qualitative interpretation of the polarization distributions.

Image analysis

Images were analyzed with ADEMSCode [37], a home-written package in MATLAB (Mathworks), to identify candidate foci corresponding to fluorescent complexes. The super-resolved positions of the spots with an integral signal-to-noise ratio (SNR) minimum of 0.4 for mGFP assays was taken and used for custom Python post-processing. Specifically, the full frame was split into two rectangular regions of interest and the translation-only mapping between them found with scikit-image's *phase_cross_correlation* function. Not only was this mapping used to transform the images of the second channel onto the first, but also to shift the channel 2 spots into their locations in channel 1. The integrated intensity of each fluorescent focus in each channel was found by summing the intensity inside a circular mask of radius 5 pixels centered on the super-resolved position after local background correction. The local background was calculated as the mean average of pixels specified by a bitwise XOR between the circular spot mask and a square of side length 12 pixels also centered on the fluorescent focus locus. The corresponding values in both channels for a given fluorescent focus were used to calculate the polarization $\rho = (I_1 - I_2)/(I_1 + I_2)$. Together with the masks, these values were also used to plot polarization heatmaps. To avoid double counting of fluorescent foci visible in both channels, any candidates in channel 2 closer than 2 pixels to any candidate in channel 1 were neglected. All plots were made with *matplotlib*. The schematic of this process is shown in Figure 3.

We found that the emission polarization distribution appeared to vary spatially in a similar manner to the intensity of the incident laser, whose beam profile underfills the field of view. Specifically, we found that outside the central illuminated region the polarization was skewed positive, while in the center the skew appears negative. The outer region is not illuminated by the laser and therefore must be an artifact not corresponding solely to the ratio of emitted fluorescence. The negative skew in the center cannot similarly be dismissed, although the background in channel 2 (vertically polarized) is everywhere significantly larger than channel 1 (horizontally polarized) (Figure 4 a,b) which suggests a negative bias in the polarization signal that may not be fully compensated by our existing method of background subtraction.

We restricted our downstream analysis to the fluorescent foci lying within a radius equal to the full width at half maximum of the beam, within which the excitation intensity (and the expected total emission intensity) is relatively high. In practice this radius is approximately 90 pixels or 4.8 µm in the sample plane.

Results

Vertically, horizontally, and circularly polarized light give different distributions for mGFP immobilized in vitro

We began by immobilizing mGFP as in the protocol in Figure 2, and imaging with the excitation beam polarized either vertically, horizontally, or circularly. We acquired >10 fields of view in each case and analyzed as above. In Figure 4 we present representative fields of view under circularly polarized excitation (Figure 4 a,b) and extracted a polarization heatmap (Figure 4c). It is possible to resolve the apparent net polarizations of individual mGFP molecules at this imaging speed, despite the large uncertainty (up to 50%) in their total emission intensity. We see that in the cases of vertically and horizontally polarized excitation (Figure 4 panels d and e respectively) there are distinct distributions (Kolmogorov-Smirnov (KS) test [45], $p < 0.01$) which are skewed towards the polarization of the excitation laser as expected (positive for horizontal and negative for vertical, Table 1).

	H	V	C	$\frac{H+V}{2}$	C (fd.)
H					
V	0.008				
C	0.7	0.02			
$\frac{H+V}{2}$	0.06	0.8	0.1		
C (fd.)	0.1	0.003	0.2	0.03	

Table 1: Two-sample Kolmogorov–Smirnov test (MATLAB *kstest*) of dissimilarity of polarization distributions, showing *p* significance values. Labels refer to the following datasets: immobile mGFP imaged with horizontally (*H*), vertically (*V*) or circularly (*C*) polarized excitation, or freely diffusing mGFP imaged with circularly polarized excitation (*C*, fd.). Very low values $p < 0.1$ (black) imply a significant difference such as a shift in median, while moderate values around p = 0.1 (grey) may result from a similar median but different variance, or *vice versa*. High values, p >> 0.1, indicate that the test cannot separate the distributions. The C distributions appear more similar to *H* than to *V*, due to the negative polarization bias in measurement.

Physically, this arises because of photoselection, whereby fluorophores aligned parallel to the polarization of the excitation laser are more likely to be excited than those aligned perpendicularly. This leads to a higher rate of detection of aligned fluorophores and the distribution overall is therefore skewed towards the excitation polarization. The magnitude of photoselection bias here is expected to be about $\rho = \pm 0.3$, qualitatively consistent with observation. Quantitatively, however, we cannot exclude the presence of confounding factors of a similar magnitude. Some are expected to average out in the distribution, such as the noise on each single-molecule polarization measurement, while others including depolarization and *G*-type correction factors will not.

Under circularly polarized excitation, symmetry considerations would suggest a distribution which is the sum of the vertical and horizontal cases, and indeed we see in Figure 4f that the circularly polarized distribution is qualitatively similar to the sum of the distributions in panels 4d and 4e (KS test, p = 0.1). This acts as a useful check on the delivery of excitation and of the consistency of detection. The shape of this distribution resolved at a high statistical power is also reassuringly symmetric around its mean, since the photoselection is equalized along both axes. However, rather than the expected mean $\langle \rho_C \rangle = 0$ for the circular polarization case, there is a consistent negative

offset, which strongly indicates a significant difference in the optical transmission efficiencies, and/or depolarization properties, of our split detection channels.

However, we are not seeking to extract detailed orientation information, and noting the differences in overall distribution for bound and free fluorophores, we can say that this source of systematic error, similar to a *G* correction factor in anisotropy instruments, does not materially affect the qualitative interpretation of our results. We intend that ongoing calibrations will act to remove these influences such that the polarization signals can be rendered independent of the instrument.

The relative proportion of fluorescence intensity in either polarization detection channel across all surface-immobilized mGFP assays we tried varied between approximately 1% and 99% as a proportion of the sum of I_1+I_2.

mGFP freely diffusing shows a distinct polarization distribution

In Figure 4g we show the overall distribution for tracking mGFP molecules freely diffusing *in vitro*. In total we tracked 10 different acquisitions for 100 frames each giving 1000 total frames of information in this case. The polarization distribution is smooth, symmetric and again centered around *ca.* ρ = -0.2, which is distinct from the immobilized mGFP cases under linear excitation (Figs 4d-e, KS test: $p < 0.1$), but with far fewer extreme values when compared to the immobilized circular excitation (Fig 4f) or the sum of the immobilized linear excitation cases (KS test, $p < 0.1$). The expectation for a freely diffusing system would be that the polarization distribution peaks around ρ = 0 regardless of excitation polarization, as the intensity in each channel should be approximately equal under rotation events during the fluorescence lifetime (which washes out any photoselection under linear excitation) and under many thousands of rotation events during the camera integration time (which mask the presence of a dipole under circular excitation).

The negative offset is manifest in a noticeable shift of the mean polarization, though the decay is symmetrical on both sides of the centre of the measured distribution. This is the expected behavior for a system with a consistent sample-independent bias in polarization measurement, likely due to rectifiable differences in the noise floors and optical properties of the two channels. Regardless of this systematic error, there is a clear similarity (KS test, $p > 0.1$) in the averages of the immobile and freely diffusing cases under circular excitation, while the tails of the distributions are qualitatively distinct. The apparently narrower distribution in the freely diffusing case would imply a more rotationally averaged dipole as expected, but this difference in variance cannot presently be separated from the contributions due to the underlying sensitivity of the measurement.

Discussion and Conclusions

In this proof-of-concept work we have extended rapid and high sensitivity Slimfield microscopy to image super-resolvable fluorophores, that are commonly employed as molecular reporters in cellular processes, with polarization information. We used our in-house fluorescent foci tracking suite of software ADEMSCode and a novel Python analysis code to automatically spatially register image channels, detect fluorophores, and measure distributions of the polarization metric

$\rho = (I_1 - I_2)/(I_1 + I_2)$, where I_1 and I_2 are the respective horizontally- and vertically-polarized components of the fluorescent emission.

For surface-immobilized fluorophores we show three distinct distributions depending on excitation polarization and demonstrate that the circularly polarized excitation gives rise to a distribution that is approximately the sum of the vertical and horizontal excitation distributions as expected. In the case of freely diffusing fluorescent protein, we used circular polarized excitation light to demonstrate that the distribution is symmetric around a small negative polarization value, which we hypothesize to be an artifact due to different noise floors between the two detection channels, in contrast to previous studies in which the polarization is split by a single prism [46]. The freely diffusing case is distinct from the surface-immobilized one, indicating that even at relatively long at 40 ms exposure time compared against ns rotational timescales in free solution, our instrument is sensitive to the difference in fluorophore dynamics. With brighter artificial dyes, or improved sensitivity such as through modelling of depolarization effects, we may be able to go to lower exposure times and gain more information on the fluorophores such as diffusion coefficients, and aim to use this methodology on live cells, though this is beyond the scope of the present introductory work. Although the range of power in either polarization detection channel is 1-99% the minimum intensity of the *brightest* focus from either I_1 or I_2 never goes below 50%. Since the analysis software uses the brightest detected focus from either channel to pinpoint the location of the fluorescent emitter this is what ultimately determines the lateral spatial precision. In our imaging regime, the lateral precision scales approximately as the reciprocal of the square root of the number of photons. From the number of photons detected per fluorophore relative to our regular Slimfield we therefore estimate that the lateral precision is at worst ~60 nm.

Finally, we note that this assay gives information on whether an individual target fluorophore is bound or unbound to a substrate with high spatial (super-resolved over tens of microns) and competitive temporal resolution (tens of ms). Presently, it does not provide the level of sensitivity to anisotropy available in ensemble techniques, though this has a significant scope for improvement. Most notably, we use a relatively coarse analysis which only corrects for local background in each channel and does not yet fully represent the potential information contained in the images. We do not here correct for depolarization effects either in the excitation or imaging paths. In future we aim to perform more extensive and rigorously controlled calibration such that we can approximate a correction for the polarization measurement (including, but not limited to, accommodations equivalent to the instrument's *G* correction factor used in ensemble assays). Based on the speed, scale and sensitivity of our imaging method, there is future potential to extract time-resolved orientations for single molecules tracked with non-specialist, extensible, super-resolved Slimfield microscopy. Once this is complete, we can move to imaging *in vivo* and eventually beyond whole organelle or whole molecular complex imaging to photobleaching and measurement of individual molecules *in vivo,* extracting a host of information such as molecular stoichiometry and diffusion coefficients, which not only describe biologically relevant molecular complexes, but allow us to unpick their mechanistic relevance in living cells. Our technique represents a first step towards developing a useful and simple to implement tool for probing the dynamical properties of molecules *in vivo* and a new avenue for understanding the physics that underlies life.

Acknowledgements We thank Dr Ji-Eun Lee for assistance with microscopy.

Funding Work was supported by the Leverhulme Trust (grant RPG-2019-156) and the Engineering and Physical Sciences Research Council EPSRC (grant EP/T002166/1).

References

[1] M. C. Leake, “The physics of life: One molecule at a time,” *Philos. Trans. R. Soc. B Biol. Sci.*, vol. 368, no. 1611, p. 20120248, Feb. 2013, doi: 10.1098/rstb.2012.0248.

[2] A. J. M. Wollman, R. Nudd, E. G. Hedlund, and M. C. Leake, “From animaculum to single molecules: 300 years of the light microscope,” *Open Biol.*, vol. 5, no. 4, pp. 150019–150019, Apr. 2015, doi: 10.1098/rsob.150019.

[3] H. Miller, Z. Zhou, J. Shepherd, A. J. M. Wollman, and M. C. Leake, “Single-molecule techniques in biophysics: A review of the progress in methods and applications,” *Reports Prog. Phys.*, vol. 81, no. 2, p. 24601, 2018, doi: 10.1088/1361-6633/aa8a02.

[4] P. E. Smith and W. F. van Gunsteren, “Translational and Rotational Diffusion of Proteins,” *J. Mol. Biol.*, vol. 236, no. 2, pp. 629–636, 1994, doi: https://doi.org/10.1006/jmbi.1994.1172.

[5] V. Wong and D. A. Case, “Evaluating Rotational Diffusion from Protein MD Simulations,” *J. Phys. Chem. B*, vol. 112, no. 19, pp. 6013–6024, May 2008, doi: 10.1021/jp0761564.

[6] G. Rivas and A. P. Minton, “Macromolecular Crowding In Vitro, In Vivo, and In Between,” *Trends in Biochemical Sciences*. 2016, doi: 10.1016/j.tibs.2016.08.013.

[7] M. Roos *et al.*, “Coupling and Decoupling of Rotational and Translational Diffusion of Proteins under Crowding Conditions,” *J. Am. Chem. Soc.*, 2016, doi: 10.1021/jacs.6b06615.

[8] T. Ha, T. A. Laurence, D. S. Chemla, and S. Weiss, “Polarization Spectroscopy of Single Fluorescent Molecules,” *J. Phys. Chem. B*, vol. 103, no. 33, pp. 6839–6850, Aug. 1999, doi: 10.1021/jp990948j.

[9] C. C. Gradinaru, D. O. Marushchak, M. Samim, and U. J. Krull, “Fluorescence anisotropy: from single molecules to live cells,” *Analyst*, vol. 135, no. 3, pp. 452–459, 2010, doi: 10.1039/B920242K.

[10] G. Weber, “Rotational Brownian Motion and Polarization of the Fluorescence of Solutions,” *Adv. Protein Chem.*, 1953, doi: 10.1016/S0065-3233(08)60096-0.

[11] D. M. Warshaw *et al.*, “Myosin conformational states determined by single fluorophore polarization,” *Proc. Natl. Acad. Sci.*, vol. 95, no. 14, pp. 8034 LP – 8039, Jul. 1998, doi: 10.1073/pnas.95.14.8034.

[12] G. S. Harms, M. Sonnleitner, G. J. Schütz, H. J. Gruber, and T. Schmidt, “Single-Molecule Anisotropy Imaging,” *Biophys. J.*, vol. 77, no. 5, pp. 2864–2870, Nov. 1999, doi: 10.1016/S0006-3495(99)77118-3.

[13] H. Miller *et al.*, “High-speed single-molecule tracking of CXCL13 in the B-follicle,” *Front. Immunol.*, 2018, doi: 10.3389/fimmu.2018.01073.

[14] J. Cosgrove *et al.*, “B cell zone reticular cell microenvironments shape CXCL13 gradient formation,” *Nat. Commun.*, vol. 11, no. 1, pp. 1–15, 2020, doi: 10.1038/s41467-020-17135-2.

[15] B. Bowen and N. Woodbury, “Single-molecule fluorescence lifetime and anisotropy measurements of the red fluorescent protein, DsRed, in solution.,” *Photochem. Photobiol.*, vol. 77, no. 4, pp. 362–369, Apr. 2003, doi: 10.1562/0031-8655(2003)077<0362:sflaam>2.0.co;2.

[16] S. M. Burrows and D. Pappas, “Measuring complexation by single-molecule fluorescence

anisotropy," *Analyst*, vol. 133, no. 7, pp. 870–873, 2008, doi: 10.1039/B800110C.

[17] A. S. Backer, M. Y. Lee, and W. E. Moerner, "Enhanced DNA imaging using super-resolution microscopy and simultaneous single-molecule orientation measurements," *Optica*, 2016, doi: 10.1364/optica.3.000659.

[18] A. S. Backer, A. S. Biebricher, G. A. King, G. J. L. Wuite, I. Heller, and E. J. G. Peterman, "Single-molecule polarization microscopy of DNA intercalators sheds light on the structure of S-DNA," *Sci. Adv.*, 2019, doi: 10.1126/sciadv.aav1083.

[19] T. P. Burghardt, K. Ajtai, D. K. Chan, M. F. Halstead, J. Li, and Y. Zheng, "GFP-tagged regulatory light chain monitors single myosin lever-arm orientation in a muscle fiber," *Biophys. J.*, 2007, doi: 10.1529/biophysj.107.107433.

[20] A. Kress *et al.*, "Mapping the Local Organization of Cell Membranes Using Excitation-Polarization-Resolved Confocal Fluorescence Microscopy," *Biophys. J.*, vol. 105, no. 1, pp. 127–136, 2013, doi: https://doi.org/10.1016/j.bpj.2013.05.043.

[21] C. Vinegoni, P. F. Feruglio, I. Gryczynski, R. Mazitschek, and R. Weissleder, "Fluorescence anisotropy imaging in drug discovery," *Advanced Drug Delivery Reviews*. 2019, doi: 10.1016/j.addr.2018.01.019.

[22] D. Jameson and J. Croney, "Fluorescence Polarization: Past, Present and Future," *Comb. Chem. High Throughput Screen.*, 2012, doi: 10.2174/138620703106298347.

[23] D. Sinha, S. Sastry, and G. V. Shivashankar, "Probing messenger RNA conformational heterogeneity using single-molecule fluorescence anisotropy," *Appl. Phys. Lett.*, vol. 88, no. 10, p. 103901, Mar. 2006, doi: 10.1063/1.2183358.

[24] R. Iizuka, T. Ueno, N. Morone, and T. Funatsu, "Single-Molecule Fluorescence Polarization Study of Conformational Change in Archaeal Group II Chaperonin," *PLoS One*, vol. 6, no. 7, p. e22253, Jul. 2011, doi: 10.1371/journal.pone.0022253.

[25] A. H. Gough and D. L. Taylor, "Fluorescence anisotropy imaging microscopy maps calmodulin binding during cellular contraction and locomotion," *J. Cell Biol.*, 1993, doi: 10.1083/jcb.121.5.1095.

[26] D. M. Jameson and J. A. Ross, "Fluorescence polarization/anisotropy in diagnostics and imaging," *Chem. Rev.*, 2010, doi: 10.1021/cr900267p.

[27] H. A. Shaban *et al.*, "Polarized Resolved Single-Molecule Localization-Based Super-Resolution Fluorescence Microscopy Reveals Orientation Order in Bio-Molecular Assemblies," *Biophys. J.*, vol. 106, no. 2, pp. 203a-204a, Jan. 2014, doi: 10.1016/j.bpj.2013.11.1196.

[28] J. N. Forkey, M. E. Quinlan, and Y. E. Goldman, "Measurement of Single Macromolecule Orientation by Total Internal Reflection Fluorescence Polarization Microscopy," *Biophys. J.*, vol. 89, no. 2, pp. 1261–1271, Aug. 2005, doi: 10.1529/biophysj.104.053470.

[29] M. P. Backlund *et al.*, "Removing orientation-induced localization biases in single-molecule microscopy using a broadband metasurface mask," *Nat. Photonics*, vol. 10, no. 7, pp. 459–462, May 2016, doi: 10.1038/nphoton.2016.93.

[30] O. Nevskyi, R. Tsukanov, I. Gregor, N. Karedla, and J. Enderlein, "Fluorescence polarization filtering for accurate single molecule localization," *APL Photonics*, vol. 5, no. 6, p. 61302, Jun. 2020, doi: 10.1063/5.0009904.

[31] S. B. Mehta *et al.*, "Dissection of molecular assembly dynamics by tracking orientation and position of single molecules in live cells," *Proc. Natl. Acad. Sci. U. S. A.*, 2016, doi:

10.1073/pnas.1607674113.

[32] L. Chen *et al.*, “Advances of super-resolution fluorescence polarization microscopy and its applications in life sciences,” *Comput. Struct. Biotechnol. J.*, vol. 18, pp. 2209–2216, 2020, doi: 10.1016/j.csbj.2020.06.038.

[33] J. F. Beausang, Y. E. Goldman, and P. C. Nelson, “Changepoint Analysis for Single-Molecule Polarized Total Internal Reflection Fluorescence Microscopy Experiments,” 2011, pp. 431–463.

[34] A. H. A. Clayton, Q. S. Hanley, D. J. Arndt-Jovin, V. Subramaniam, and T. M. Jovin, “Dynamic Fluorescence Anisotropy Imaging Microscopy inthe Frequency Domain (rFLIM),” *Biophys. J.*, vol. 83, no. 3, pp. 1631–1649, Sep. 2002, doi: 10.1016/S0006-3495(02)73932-5.

[35] A. S. Backer and W. E. Moerner, “Determining the rotational mobility of a single molecule from a single image: a numerical study,” *Opt. Express*, vol. 23, no. 4, p. 4255, Feb. 2015, doi: 10.1364/OE.23.004255.

[36] M. Plank, G. H. Wadhams, and M. C. Leake, “Millisecond timescale slimfield imaging and automated quantification of single fluorescent protein molecules for use in probing complex biological processes,” *Integr. Biol.*, vol. 1, no. 10, pp. 602–612, Oct. 2009, doi: 10.1039/b907837a.

[37] H. Miller, Z. Zhou, A. J. M. Wollman, and M. C. Leake, “Superresolution imaging of single DNA molecules using stochastic photoblinking of minor groove and intercalating dyes,” *Methods*, vol. 88, pp. 81–88, Jan. 2015, doi: 10.1016/j.ymeth.2015.01.010.

[38] A. J. M. Wollman and M. C. Leake, “Millisecond single-molecule localization microscopy combined with convolution analysis and automated image segmentation to determine protein concentrations in complexly structured, functional cells, one cell at a time,” *Faraday Discuss.*, vol. 184, no. 0, pp. 401–424, 2015, doi: 10.1039/c5fd00077g.

[39] A. J. M. Wollman, S. Shashkova, E. G. Hedlund, R. Friemann, S. Hohmann, and M. C. Leake, “Transcription factor clusters regulate genes in eukaryotic cells,” *Elife*, vol. 6, pp. 1–36, 2017, doi: 10.7554/eLife.27451.

[40] A. H. Syeda *et al.*, “Single-molecule live cell imaging of Rep reveals the dynamic interplay between an accessory replicative helicase and the replisome,” *Nucleic Acids Res.*, vol. 47, no. 12, pp. 6287–6298, 2019, doi: 10.1093/nar/gkz298.

[41] M. C. Leake, J. H. Chandler, G. H. Wadhams, F. Bai, R. M. Berry, and J. P. Armitage, “Stoichiometry and turnover in single, functioning membrane protein complexes,” *Nature*, vol. 443, no. 7109, pp. 355–358, Sep. 2006, doi: 10.1038/nature05135.

[42] T. D. M. Bell and A. H. A. Clayton, “The transition from single molecule to ensemble revealed by fluorescence polarization.,” *Sci. Rep.*, 2015, doi: 10.1038/srep08158.

[43] M. Deutsch, R. Tirosh, M. Kaufman, N. Zurgil, and A. Weinreb, “Fluorescence Polarization as a Functional Parameter in Monitoring Living Cells: Theory and Practice,” in *Journal of Fluorescence*, 2002, doi: 10.1023/A:1015355018449.

[44] F. T. S. Chan, C. F. Kaminski, and G. S. K. Schierle, “HomoFRET fluorescence anisotropy imaging as a tool to study molecular self-assembly in live cells,” *ChemPhysChem*. 2011, doi: 10.1002/cphc.201000833.

[45] M. Marozzi, “Nonparametric Simultaneous Tests for Location and Scale Testing: A Comparison of Several Methods,” *Commun. Stat. - Simul. Comput.*, vol. 42, no. 6, pp. 1298–

1317, Jul. 2013, doi: 10.1080/03610918.2012.665546.

[46] C. A. V. Cruz *et al.*, "Quantitative nanoscale imaging of orientational order in biological filaments by polarized superresolution microscopy," *Proc. Natl. Acad. Sci. U. S. A.*, 2016, doi: 10.1073/pnas.1516811113.

Figures and captions

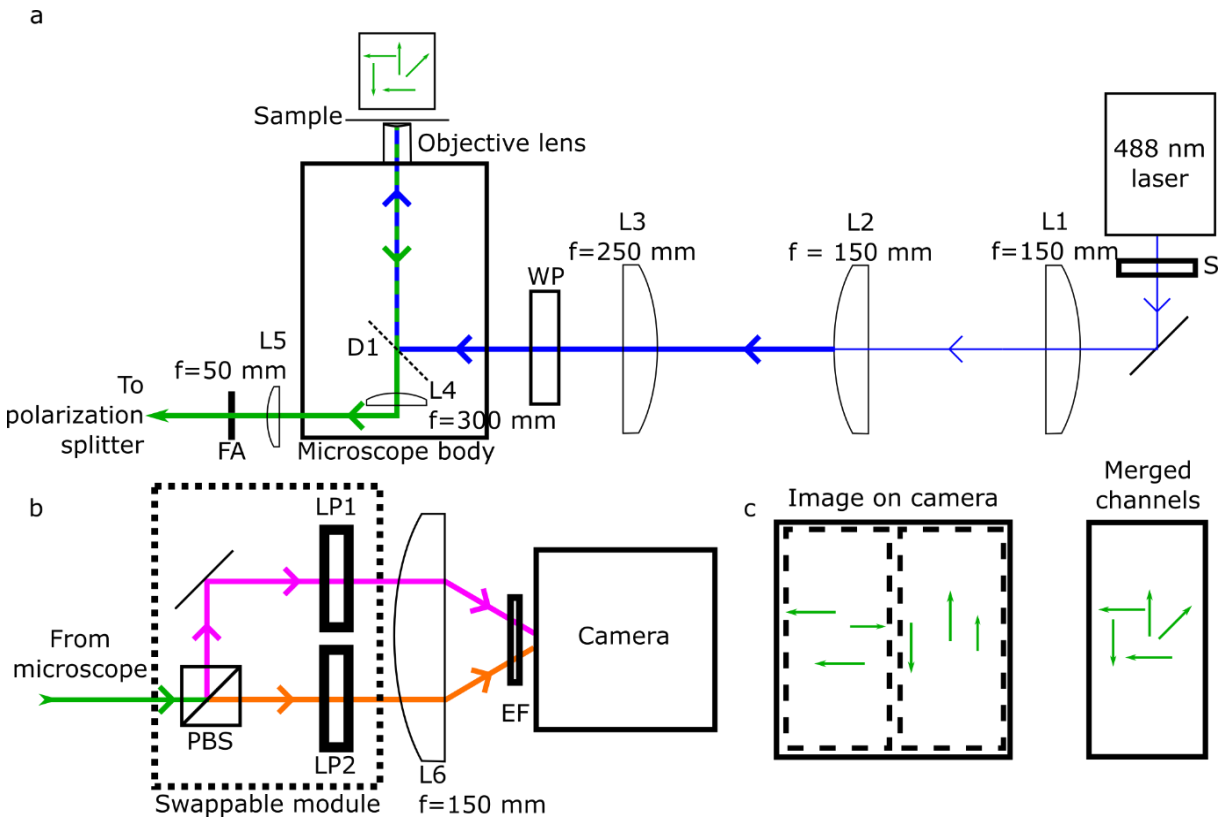

Figure 1. Schematic diagram of the Slimfield microscope. *a*) Laser light vertically polarized at source (blue) passes through a shutter (S) and is expanded 3x by the lens pair L1 and L2, before passing through L3 which forms a telescope with the objective lens to ensure light at the sample is collimated. Finally, in the excitation path the laser light passes through a wave plate (WP) on a rotational mount, either λ/2 for linear polarization or λ/4 for circular polarization. The light is directed to the sample with a dichroic mirror which allows the collected fluorescence (green) to pass through it. The emission then encounters the lens L4 and is focused at the side port of the

microscope body to form an intermediate image plane into which we place adjustable slits to provide a rectangular field aperture (FA). The emission is then recollimated with the lens L5; *b*) The image light then encounters the polarization splitting module and the vertical and horizontal polarized light (orange and pink respectively) are separated by a broadband, polarizing beamsplitter cube. Each polarization channel then is purified by a linear polarization filter (LP1 and LP2) before being focused on to the left and right sides of the same camera chip by the lens L6. For convenience, components inside the dotted box are mounted to a breadboard which is on removable magnetic mounts and can therefore be easily swapped for another module, e.g. color splitter. Immediately before the camera, reflected excitation light is removed by an emission filter, EF. c) The left-hand side of the acquired image shows the horizontal polarized light and the right-hand side shows the vertical (individual channels are indicated by dashed boxes). By registering the image and creating a composite image we recover the true fluorophore distribution.

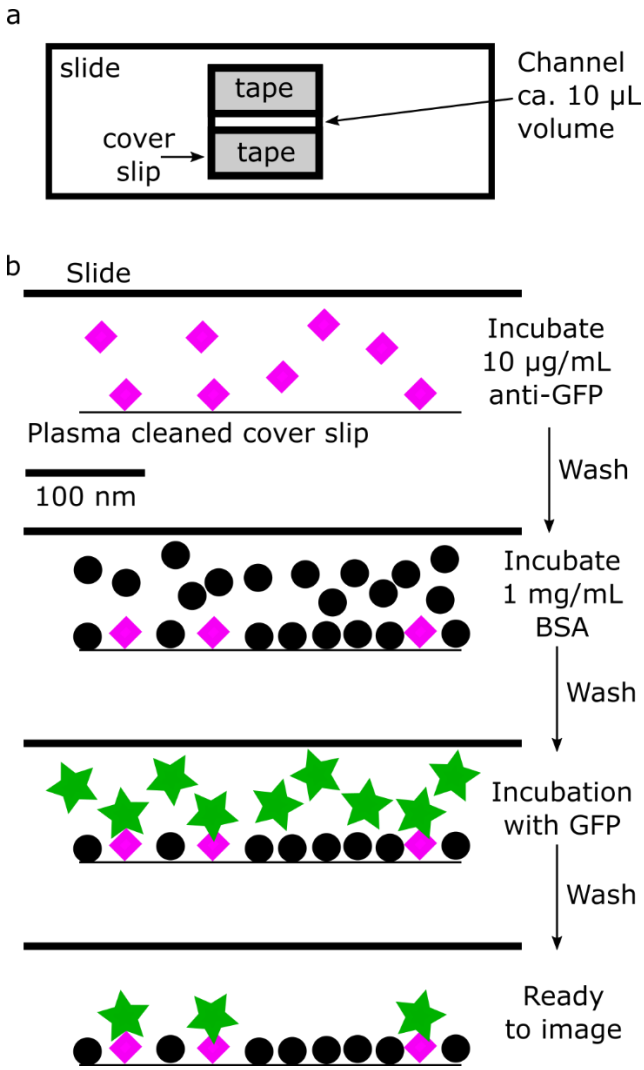

Figure 2. a) A flow cell is created with a slide, plasma cleaned cover slip, and two lengths of double-sided tape. b) Schematic of the surface immobilized mGFP assay. First, anti-GFP is introduced to the flow cell and allowed to incubate. The anti-GFP (pink diamonds) has a high affinity for the plasma cleaned surface and are readily and strongly immobilized. After washing, 1 mg/mL BSA (black circles)

is incubated to passivate the remaining exposed surface. After 5 minutes this is washed out and the mGFP itself (green stars) is introduced to bind with the anti-GFP antibody and allowed to incubate 5 minutes using a previously reported protocol [41]. After a final wash, the sample is ready to image (bottom panel). Before loading on to the sample, the channel can be hermetically sealed with nail polish or wax.

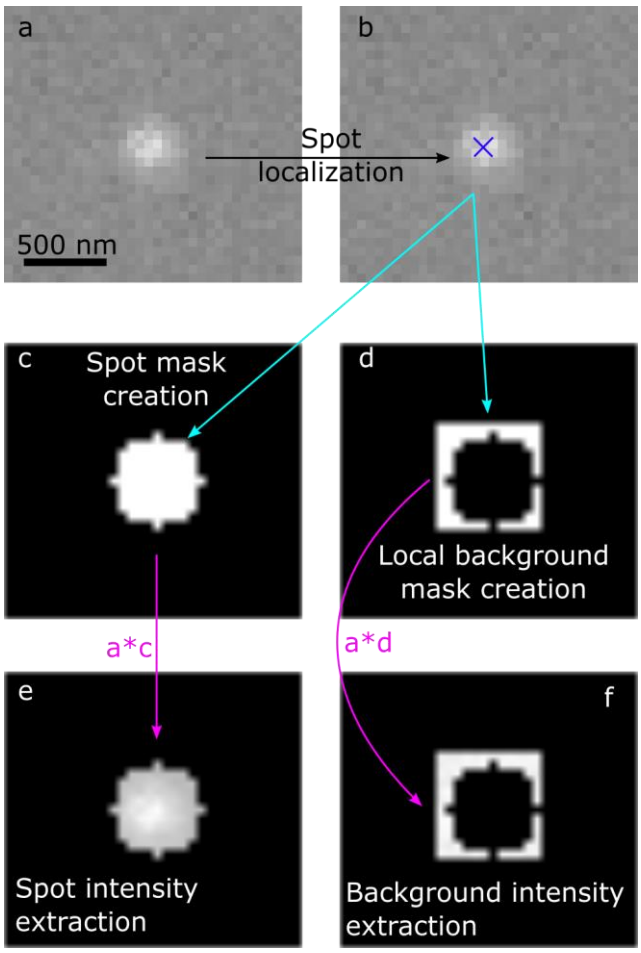

Figure 3. a) Raw data from one of the polarization channels is passed to ADEMSCode (panel b) for spot fitting and subpixel localization. This localization is used to create two masks – one for the spot itself (c) and one for the local background (d). These are multiplied by the original image to give the intensities for each (e and f). The total fluorophore intensity is then the sum of each nonzero pixel in (e) after subtraction of the mean local background fluorescence in (f).

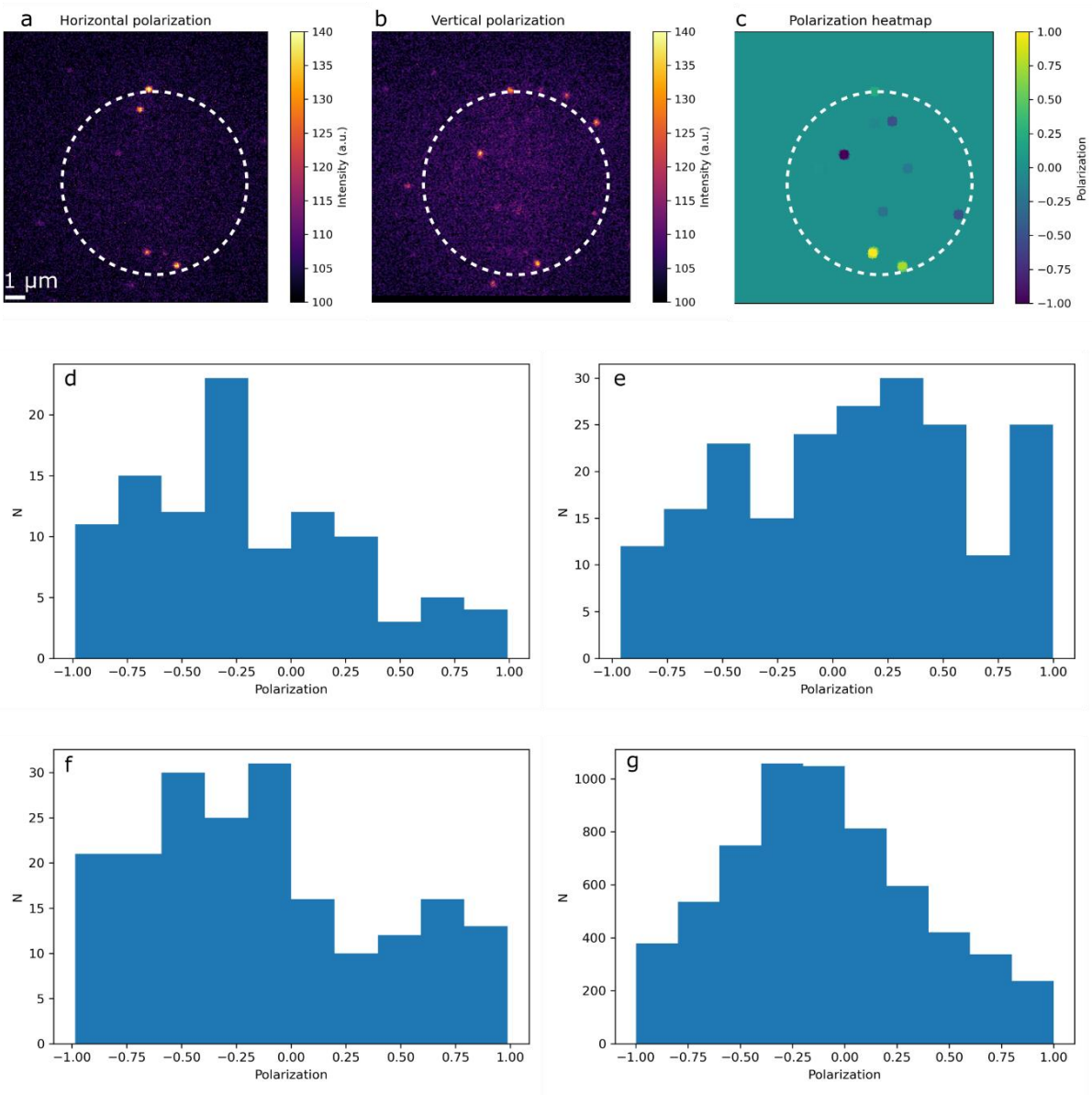

Figure 4. a) Vertical polarization channel from a representative GFP *in vitro* assay under circular polarized excitation. b) Horizontal polarization channel from the same assay as in a), both with

illuminated region of interest shown as dashed circles. c) The polarization heatmap found by combining a) and b) and analyzing as in Figure 3. d-f) Polarization distribution for surface immobilized mGFP when illuminated by d) vertically, e) horizontally and f) circularly polarized light. g) Polarization distribution for freely diffusing mGFP illuminated with circularly polarized light. Panels d-f have N = 104, 208, 195, and 6,170 tracks respectively.